nature materials

ARTICLES

https://doi.org/10.1038/s41563-018-0135-0

Structural evolution of titanium dioxide during reduction in high-pressure hydrogen

Sencer Selcuk*, Xunhua Zhao and Annabella Selloni*

The excellent photocatalytic properties of titanium oxide (TiO_2) under ultraviolet light have long motivated the search for doping strategies capable of extending its photoactivity to the visible part of the spectrum. One approach is high-pressure and high-temperature hydrogenation, which results in reduced 'black TiO_2' nanoparticles with a crystalline core and a disordered shell that absorbs visible light. Here we elucidate the formation mechanism and structural features of black TiO_2 using first-principles-validated reactive force field molecular dynamics simulations of anatase TiO_2 surfaces and nanoparticles at high temperature and under high hydrogen pressures. Simulations reveal that surface oxygen vacancies created upon reaction of H_2 with surface oxygen atoms diffuse towards the bulk material but encounter a high barrier for subsurface migration on {001} facets of the nanoparticles, which initiates surface disordering. Besides confirming that the hydrogenated amorphous shell has a key role in the photoactivity of black TiO_2, our results provide insight into the properties of the disordered surface layers that are observed on regular anatase nanocrystals under photocatalytic water-splitting conditions.

TiO_2 is one of the most chemically stable, functionally versatile and widely used oxide materials, with applications ranging from bone implants and coatings to photocatalysis and photovoltaic cells[1–4]. An insulator with a bandgap around 3 eV, TiO_2 can easily be reduced to TiO_{2-x}, an n-type semiconductor more efficient than the pristine form for many applications[5,6]. There has therefore been considerable interest in methods of generating reduced TiO_2 with improved properties in recent years[7,8]. In particular, efforts have focused on black, hydrogenated TiO_2, a material that is capable of absorbing the whole spectrum of visible light, and that has strong activity for photocatalytic H_2 evolution from water[9–14].

Black TiO_2 is typically produced by exposing nanoparticles of anatase (the TiO_2 form usually found in nanomaterials) to a 20 bar H_2 atmosphere at 200–500 °C for a time ranging from 1 to 2 hours to a few days[11–13]. The resulting reduced nanoparticles comprise a crystalline TiO_2 core and a disordered shell[9,11], whose chemical composition (degree of reduction and hydrogenation) and atomic structure (extent of disorder) have not been established in detail. A reduced and hydroxylated disordered surface layer is also observed on anatase nanocrystals under conditions relevant to photocatalytic water splitting, where hydroxyls and reduced Ti^{3+} ions are formed upon water-dissociative adsorption at photogenerated oxygen vacancies[15,16]. This suggests a direct link between the photocatalytic activity of black TiO_2 nanoparticles and formation of an amorphous layer on their surface, providing an additional motivation for an in-depth study of their structure.

Here we use classical reactive force field (ReaxFF) molecular dynamics simulations[17–19] validated by first-principles density functional theory (DFT) calculations to obtain a direct, atomistic view of the high-temperature, high-pressure hydrogenation of anatase TiO_2 and the structure of the resulting material. Unlike the conventional classical force field potentials, ReaxFF represents each element in a single, transferable way across different chemical environments to describe reactive events, such as two oxygen atoms leaving the TiO_2 surface to form a gas-phase O_2 molecule. Although ReaxFF simulations are not as accurate as first-principles molecular dynamics[19,20], with this approach one can perform simulations of systems of thousands of atoms on timescales of a few nanoseconds, which is far beyond what is currently accessible with first-principles molecular dynamics simulations[19].

Interaction of hydrogen with anatase TiO_2

Fig. 1 shows free-energy diagrams for the majority (101) surface of anatase in H_2/H_2O atmosphere obtained from ab initio thermodynamics[21] (see Methods for details). Dissociative adsorption of a H_2 molecule on anatase is approximately thermoneutral at $T = 0$ K, and it becomes thermodynamically unfavourable at finite temperatures (Fig. 1a). In contrast, the reaction between H_2 and a surface oxygen atom (O_s) of anatase to form H_2O and a surface oxygen vacancy (V_O), that is, $H_2 + O_s \rightarrow H_2O + V_O$, is endothermic at $T = 0$ K, but becomes rapidly favourable at higher temperature and low water chemical potential (Fig. 1b; see also ref. [22]), which are the conditions used for high-pressure hydrogenation of anatase.

In agreement with these DFT results, the ReaxFF simulations show rapid formation of water molecules and surface V_Os on anatase surfaces exposed to high-temperature and high-pressure H_2 atmosphere. Fig. 1c shows the typical mechanism of this process, which is also consistent with a previous DFT study[23]. On the other hand, the (reactive) force field we used overestimates the reactivity of the anatase surface. In particular, it favours dissociative adsorption of H_2 (the thermodynamically most difficult step of water formation on anatase) by as much as 2.2 eV (about 50 kcal mol^{-1}) compared to DFT. This difference is certainly a limitation of ReaxFF. However, favouring H_2 dissociation (that is, decreasing the chemical potential of adsorbed H atoms, H_{ads}) speeds up H_2O formation. Similar to using a simulation temperature larger than the experimental one, as is often done, this allows us to observe effects in our simulations that take place over a much longer timescale in the experiment. Unlike the H_2 dissociation energy, the diffusion pathways and barriers of H_{ads} predicted by the ReaxFF agree very well with the first-principles results[23] (see Supplementary Fig. 1).

Department of Chemistry, Princeton University, Princeton, NJ, USA. *e-mail: sselcuk@princeton.edu; aselloni@princeton.edu

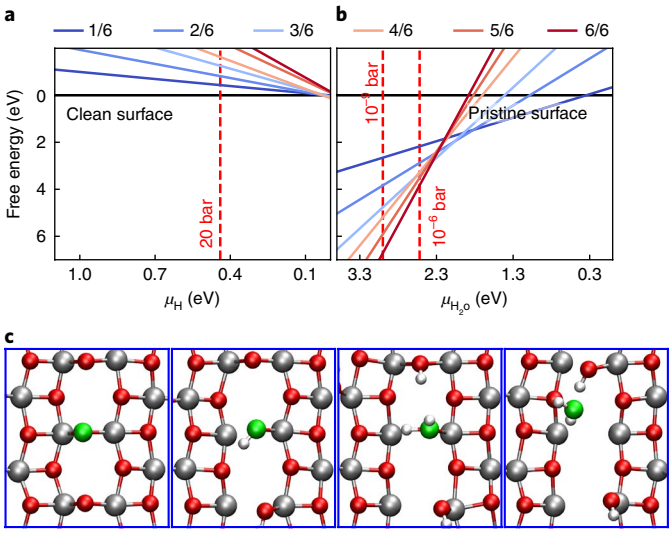

Fig. 1 | Surface stability in H_2 and mixed H_2/H_2O atmosphere from ab initio thermodynamics calculations. a,b, Computed free energies of the a-101 surface with various coverages of adsorbed hydrogen (**a**) and surface V_Os (**b**), after the reaction $H_2 + O_s \rightarrow H_2O + V_O$. Dashed red lines indicate values of hydrogen (**a**) and water chemical potentials (**b**) typically used for the preparation of black TiO_2. **c**, Mechanism of water formation on a-101 (top view, first panel) observed in our ReaxFF simulations: an OH group formed upon dissociative adsorption of an H_2 molecule (second panel) reacts with an H resulting from the dissociation of another H_2 at a nearby oxygen site to form a water molecule (third panel), which desorbs leaving a surface V_O (fourth panel). For better clarity, only the atoms in the surface top layer are shown, and the O atom undergoing the reaction is highlighted in green.

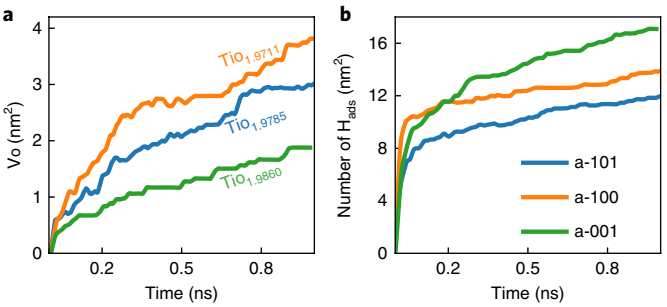

Fig. 2 | Time evolution of the reduction process in slabs exposing different surfaces. a,b, Total numbers of V_Os (**a**) and H_{ads} (**b**) per nm^2 in the a-101, a-100 and a-001 slabs in the $T = 800$ K, $p = 200$ bar H_2 atmosphere as a function of the simulation time. Neither V_Os nor H_{ads} are limited to surface layers.

Hydrogenation of extended (101), (100) and (001) surfaces

As anatase surfaces often exhibit remarkably distinct behaviour[24–27], we performed simulations on the three most common low-index (101), (001) and (100) surfaces (a-101, a-001 and a-100, respectively) at high temperature ($T = 800$ K) and under high-pressure H_2 atmosphere ($p = 200$ bar; see Methods for details). Fig. 2a shows the time evolution of the number of V_Os per surface area of the corresponding slabs during these simulations. V_O formation is easiest on the a-100 surface, where this process is more than twice as fast as that on the a-001 surface. In 1 ns, a-100, a-101 and a-001 slabs with similar shapes were reduced to $TiO_{1.9711}$, $TiO_{1.9785}$ and $TiO_{1.9860}$, respectively. Fig. 2b shows equivalent results for the number of adsorbed H atoms (H_{ads}), where the ordering changes to a-001 > a-100 > a-101. Although the numbers of H_{ads} are overestimated owing to the excessively favourable H_2 dissociation given by the ReaxFF, this ordering agrees well with previous studies of the reactivity of anatase surfaces towards adsorption of small molecules[28].

Water formation from anatase under H_2 atmosphere can only be sustained if the oxygen content of the surface layers is somehow replenished. It is known from both experiments[29] and DFT calculations[30] that V_Os are not stable on the a-101 surface; when a surface V_O is created, it promptly diffuses to the subsurface and the bulk above 200 K, thus replenishing the oxygen content of the surface. This behavior of V_Os is well reproduced by our simulations (Fig. 3a): after about 0.2 ns, V_Os start appearing in the innermost layers of the a-101 slab, and the process is even faster on the a-100 surface. Instead, essentially no subsurface diffusion of V_Os is observed on an a-001 surface, where most V_Os remain close to the surface even after a simulation time of 1 ns. Hence, unlike the a-101 and a-100 surfaces, the a-001 surface quickly becomes O-deficient. The differences in the V_O diffusion rate of different surfaces largely explain the ordering of the reduction rates in Fig. 2a.

It is interesting to elucidate why V_Os do not migrate subsurface at the a-001 surface. V_O diffusion in anatase is highly anisotropic, according to DFT calculations[30] that are well reproduced by the ReaxFF (see Supplementary Fig. 2). The barrier for the exchange of a V_O between an apical and an equatorial position of a TiO_6 octahedron is much lower than that for the exchange between two equatorial positions. As a result, V_Os diffuse easily along [100] ($\equiv$ [010] $\neq$ [001], owing to the tetragonal symmetry of the material) through zig-zag elementary steps along [301] and [30$\bar{1}$] ($\equiv$ [031] and [03$\bar{1}$]). As [100] and [010] are parallel to the a-001 surface, the V_Os formed on this surface can only diffuse laterally and their diffusion toward the bulk is largely suppressed. Fig. 3b shows snapshots from our slab simulations for all three surfaces highlighting the V_O diffusion direction. The zig-zag motion at the a-101 surface can be seen clearly in Supplementary Video 1.

Unlike V_Os, diffusion of H_{ads} toward the bulk does not exhibit a significant facet-dependence (Fig. 2b and Supplementary Fig. 3). On all surfaces, H_{ads} diffusion to the subsurface and bulk is limited, and at the end of 1 ns there is barely any H atom deeper than 1 nm below the surface. To understand this behaviour, we computed the minimum energy pathway for surface-to-subsurface H_{ads} diffusion in an a-101 slab. In agreement with first-principles calculations (Supplementary Fig. 1)[23], the overall H_{ads} diffusion barrier of about 1.1 eV is found to be several times larger than the barrier of V_O diffusion along [100], explaining the limited H incorporation in the system. This barrier is also significantly larger than the computed barriers of H_{ads} diffusion among bulk layers (about 0.5 to 0.8 eV in ReaxFF, not shown), indicating that surface-to-subsurface diffusion is the rate-limiting step of H incorporation in this material.

Hydrogenation of spherical and faceted nanoparticles

Although they provide valuable insight into the characteristics of different facets, periodic slab calculations are not sufficient to describe the behaviour in nanoparticles. For example, the V_O accumulation observed in the extended a-001 surface is unlikely to occur on a nanoparticle with small {001} facets, where edge and corner effects become important. To explicitly account for such effects, we prepared one spherical and two faceted nanoparticle models as described in the Methods (see Supplementary Figs. 4 and 15). We first tested the stability of the nanoparticles by simulating their behaviour at 800 K in vacuum. As shown in Fig. 4 for the case of the spherical nanoparticle, in 1 ns only a few V_Os were formed (Fig. 4a) and the crystal structure was preserved with relatively small overall displacement of the surface atoms (Fig. 4b). When exposed to a 200 bar H_2 atmosphere, instead, the reduction of the spherical nanoparticle was rapid even compared to the slab models under the same conditions, possibly owing to the larger surface-to-volume ratio, and the overall stoichiometry after 1 ns was $TiO_{1.9452}$

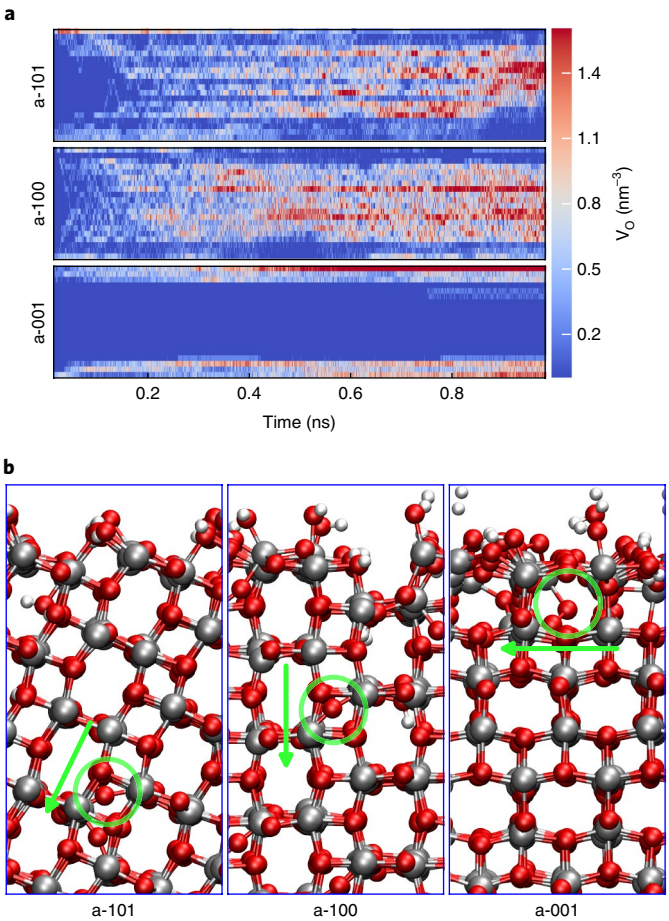

Fig. 3 | Diffusion and distribution of oxygen vacancies in slabs exposing different surfaces. a, Planar average of the V_O concentration along the surface normal direction (vertical axis) of the a-101, a-100 and a-001 slabs as a function of simulation time (horizontal axis). The initial '>'-like shape in the V_O distribution for the a-101 and a-100 slabs is due to V_O diffusion into the bulk. **b**, Atomistic details of the diffusion of V_Os formed on the different surfaces: arrows indicate the diffusion direction, which is [100] in all cases; the circled O atoms are moving in the opposite direction to fill the V_O sites.

(Fig. 4a). The right panel in Fig. 4b shows that, under these conditions, the atoms in the surface layer are displaced on average by 2–2.5 Å, a distance larger than the typical Ti–O bond length. As a result, a disordered phase is formed on the spherical nanoparticle surface, while the crystal structure is preserved immediately below (Fig. 4b,c).

Identifying V_Os is not straightforward in the disordered regions of the nanoparticles. To locate V_Os and monitor their evolution during the simulation, we employed an algorithm that matches each atom (except those in the gas phase) in a particular frame of the simulation with one in the initial structure (refer to Supplementary Information for details). The O atoms in the initial structure that cannot be mapped to an atom in the frame of interest are defined as V_Os in that frame. Fig. 5a shows the spatial distribution of V_Os in the spherical nanoparticle during the final 20 ps of a 1 ns simulation coloured according to their residency time. V_Os reside longer on sites closer to the surface, while they are more mobile in the bulk of the nanoparticle (see Supplementary Video 2 for the full time evolution). We computed the diffusion coefficient of V_Os (D_V) as well as the oxygen self-diffusion coefficient (D_O) from their respective mean squared displacements (Supplementary Fig. 12). Experimental values of D_V and D_O are not available for anatase, probably because this polymorph is not stable at the high temperatures that are typically used for such measurements. However, our results, $D_V = 8.6 \times 10^{-6}$ cm^2 s^{-1} and $D_O = 1.2 \times 10^{-8}$ cm^2 s^{-1} at $T = 800$ K, are in reasonable agreement with experimental values for $SrTiO_3$ ($D_V = 1.6 \times 10^{-6}$ cm^2 s^{-1}, $D_O = 1 \times 10^{-9}$–1×10^{-11} cm^2 s^{-1})[31] and reduced rutile TiO_2 ($D_V = 2.5 \times 10^{-6}$ cm^2 s^{-1})[32], two related oxide materials.

A remarkable result displayed in Fig. 5a is the apparent lack of V_Os near the {001} facets of the spherical nanoparticle. Closer inspection of our simulation trajectories reveals, however, that V_Os do actually form on the {001} facets of the spherical nanoparticle, but they are rapidly healed by O atoms diffusing from neighbouring surfaces, as shown by the overall displacement vectors of O atoms during the simulation (Supplementary Fig. 6). The displacement vectors do not show any preferential direction near {100} facets, whereas a net flux of O atoms directed towards {001} facets is observed. Lack of a similar observation in the simulations done in vacuum unambiguously links this phenomenon with V_O formation on {001} facets. Importantly, this process appears also to nucleate the amorphization of the nanoparticle surface. Fig. 5b shows the root mean squared displacement (RMSD) of the surface atoms projected onto the (010) plane in the early (left) and late (right) stages of the simulation. Initially, only the atoms close to the two {001} facets are displaced significantly, and the crystalline surface structure is preserved over the rest of the spherical nanoparticle. During the simulation, however, the size of the disordered region grew steadily from these two nucleation sites until it extended to the whole spherical nanoparticle surface (Supplementary Video 3).

The key role of V_Os at {001} facets in the amorphization of the spherical nanoparticle's surface is confirmed by simulations of two faceted nanoparticles that have the characteristic truncated bipyramid shape of anatase crystals with different aspect ratios (Supplementary Fig. 15)[28,33]. As shown in Supplementary Fig. 16, the extent of disorder (measured by RMSD) on the {001} facets of the truncated nanoparticle is roughly twice that of the {101} ones. In addition, the RMSD is much larger on the {101} surfaces of the truncated nanoparticle in comparison to the same surfaces of the diamond-like nanoparticle, which do not have neighbouring {001}. As found for the spherical nanoparticle, the V_O spatial distribution in the faceted nanoparticles shows a depletion of V_Os near {001} facets even towards the end of the simulation when the nanoparticle is fairly reduced (see Supplementary Fig. 17). In all three nanoparticle models, however, the total V_O concentration is highest on the surface layer, where V_Os are formed continuously (Supplementary Fig. 18). In the spherical nanoparticle and the diamond-like nanoparticle, a large fraction of the V_Os is in the inner layers, while in the truncated nanoparticle V_O concentration decreases with the depth from surface, probably because of the large V_O diffusion barrier along [001].

Unlike the behaviour of V_Os, H incorporation into the spherical nanoparticle does not show any significant difference with respect to the extended slab models (Supplementary Fig. 5). In particular, H_{ads} are mostly located in the surface shell and only a small concentration of H atoms diffused about 1 nm deep into the spherical nanoparticle during a simulation of 1 ns. The dependence of H diffusion on facet orientation is weak, so that the concentration of incorporated H is essentially isotropic.

Electronic properties

One of the most important characteristics of black TiO_2 is its much narrower bandgap compared to pristine anatase. Interestingly, this narrowing is found to originate primarily from an upward shift and tailing of the valence band[9,11], rather than the formation of gap states close to the conduction band minimum, as is typical in reduced TiO_2[5,6]. To verify whether the electronic properties of our simulated nanoparticles are consistent with experimental findings, we performed DFT calculations of the density of states (DOS) of large cluster models cut out from the spherical nanoparticle before

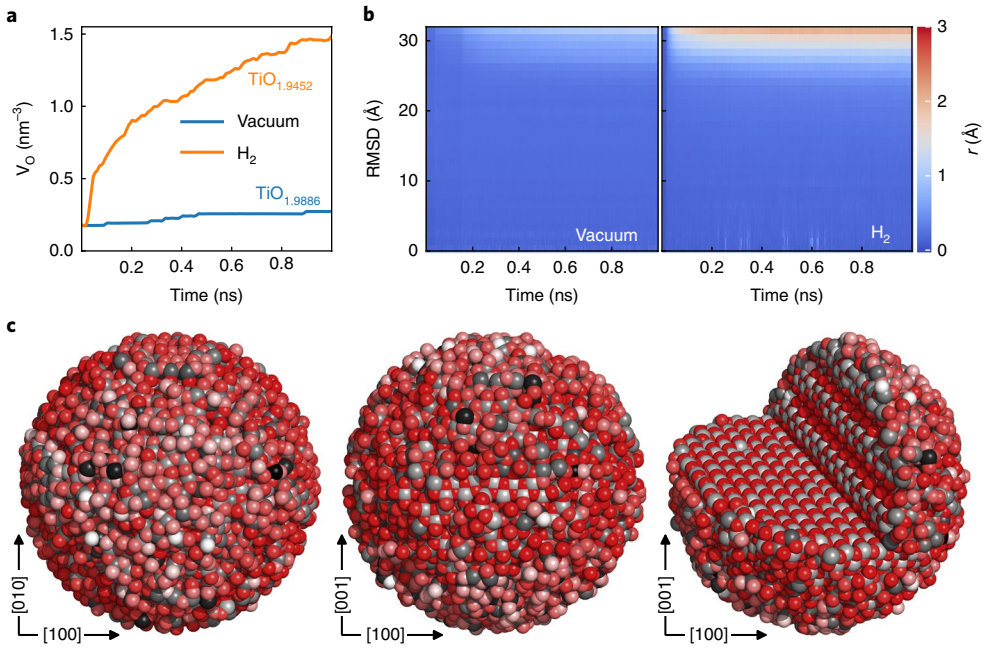

Fig. 4 | Reduction and disordering of a spherical nanoparticle during and after high-pressure hydrogenation. a, Time evolution of V_Os concentration in the spherical nanoparticle in vacuum and under H_2 atmosphere. Stoichiometric TiO_2 is taken as the reference; we note that the spherical nanoparticle is already slightly non-stoichiometric at the beginning of the simulation (see text). **b**, Time evolution of the atomic RMSD in different spherical shells. **c**, Different views of the spherical nanoparticle at the end of a 1 ns simulation under 200 bar H_2 at 800 K. The dissected view on the right shows that the crystalline anatase structure is preserved inside the spherical nanoparticle. Atoms are coloured according to their displacement from their original location: larger displacements correspond to lighter colours for O and darker colours for Ti.

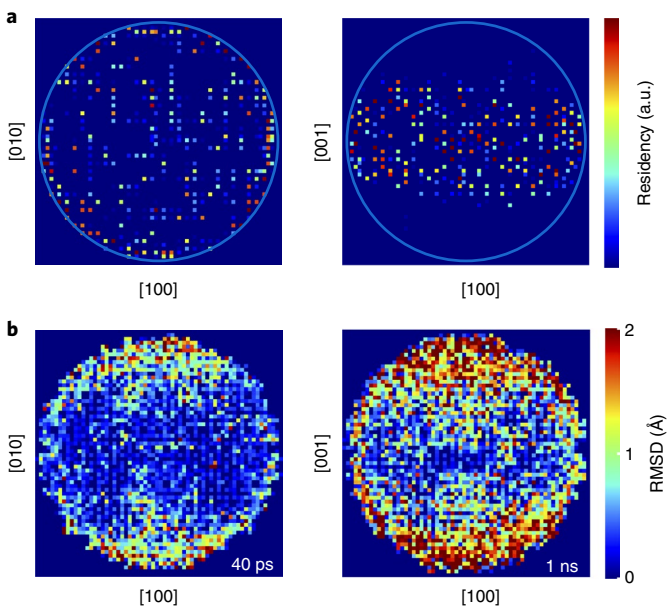

Fig. 5 | Spatial distribution of oxygen vacancies and surface disordering after hydrogenation. a, Spatial distribution of V_Os in the final 20 ps of the simulation of the spherical nanoparticle, viewed along the [001] (left) and [010] (right) directions. V_O sites are coloured according to the duration of the occupancy of that site, which highlights diffusion directions and more stable sites. Diffusion of a V_O, traced by a sequence of neighbouring pale dots, is limited to the [100] and [010] directions. The full 1 ns evolution of V_Os is shown in Supplementary Video 2. **b**, RMSD of atoms calculated over small regions at two different times. Early in the simulation (left), the disorder is large near {001} facets only, and subsequently it extends to the rest of the spherical nanoparticle surface.

and after simulation in H_2 atmosphere (see Supplementary Fig. 13). After hydrogenation, a general broadening of the bands is observed (Figs. 6a and b), together with formation of states both below and above the valence band in the shell of the nanoparticle. These states originate from OH groups and reduced Ti^{3+} ions, respectively, as expected[5]. However, different from the typical gap states of reduced TiO_2, the Ti^{3+} states in the shell of the hydrogenated nanoparticle start just above the valence band and fill most of the gap, a feature related to the large variety of chemical environments induced by the disordering (detailed structural characterization is presented in Supplementary Figs. 7–11). Moreover, analysis of the projected DOS reveals that these gap states are derived mainly from Ti 3*d* orbitals originally forming Ti–O bonding states in the valence band[34], which become destabilized when the partner oxygen atoms leave the nanoparticle. Further comparison of the DOS of the hydrogenated spherical nanoparticle to analogous calculations for bulk crystalline anatase (Fig. 6c) clearly shows the overall upward shift and tailing of the valence band in the nanoparticle relative to the ordered stoichiometric material. Agreement with the experiment is remarkable[9], indicating that the structure of our simulated nanoparticles describes the relevant features of hydrogenated black TiO_2 well.

Outlook

In summary, we have reported simulations of high-pressure hydrogenation of anatase TiO_2 nanoparticles, one of the most effective procedures for extending the photoactivity of TiO_2 to the visible, and shown that the properties of the simulated nanoparticles agree well with experimental observations for black TiO_2. Our results reveal the crucial role of different anatase surface terminations and anisotropic V_O diffusion in the formation and structure of the hydrogenated nanoparticles, confirm the critical importance of reduction and surface disorder in their properties, and also suggest that controlling the amount of a-001 surface, for which numerous procedures have already been devised[35,36], can

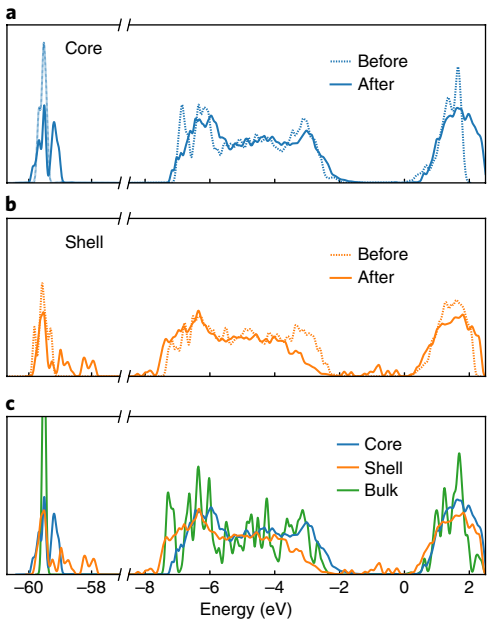

Fig. 6 | Effects of hydrogenation on the electronic DOS. a,**b**, Computed DOS for the core (**a**), and the shell (**b**) region of the investigated spherical nanoparticle before and after simulation in H_2 atmosphere at $T = 800$ K. **c**, DOS for the shell and core of the hydrogenated spherical nanoparticle are compared to the DOS of bulk crystalline anatase TiO_2. Calculations for the spherical nanoparticle were performed using representative clusters, as described in the Supplementary Information. The different DOS were aligned at the main peak of the Ti 3*s* states. All calculations were performed using the PBE + *U* method, with $U = 3.9$ eV.

be a practical tool with which to fine-tune both the reduction and the disorder. Finally, our results provide relevant insights into the structure of the hydrogenated amorphous layer that forms on anatase nanocrystals during photocatalytic water splitting[15,16] and into the effect of hydrogen treatments in other photoactive semiconducting oxides as well[37].

Methods

Methods, including statements of data availability and any associated accession codes and references, are available at https://doi.org/10.1038/s41593-017.

Received: 27 September 2017; Accepted: 15 June 2018;
Published online: 16 July 2018

References

1. Gratzel, M. Photoelectrochemical cells. *Nature* **414**, 338–344 (2001).
2. Fujishima, A., Zhang, X. & Tryk, D. A. TiO_2 photocatalysis and related surface phenomena. *Surf. Sci. Rep.* **63**, 515–582 (2008).
3. Chen, X. & Selloni, A. Introduction: titanium dioxide (TiO_2) nanomaterials. *Chem. Rev.* **114**, 9281–9282 (2014).
4. Rajh, T., Dimitrijevic, N. M., Bissonnette, M., Koritarov, T. & Konda, V. Titanium dioxide in the service of the biomedical revolution. *Chem. Rev.* **114**, 10177–10216 (2014).
5. Diebold, U. The surface science of titanium dioxide. *Surf. Sci. Rep.* **48**, 53–229 (2003).
6. Di Valentin, C., Pacchioni, G. & Selloni, A. Reduced and n-type doped TiO_2: nature of Ti^{3+} species. *J. Phys. Chem. C* **113**, 20543–20552 (2009).
7. Zuo, F. et al. Self-doped Ti^{3+} enhanced photocatalyst for hydrogen production under visible light. *J. Am. Chem. Soc.* **132**, 11856–11857 (2010).
8. Zuo, F. et al. Active facets on titanium(III)-doped TiO_2: an effective strategy to improve the visible-light photocatalytic activity. *Angew. Chem. Int. Ed.* **51**, 6223–6226 (2012).
9. Chen, X., Liu, L., Yu, P. Y. & Mao, S. S. Increasing solar absorption for photocatalysis with black hydrogenated titanium dioxide nanocrystals. *Science* **331**, 746–750 (2011).
10. Chen, X., Liu, L. & Huang, F. Black titanium dioxide (TiO_2) nanomaterials. *Chem. Soc. Rev.* **44**, 1861–1885 (2015).
11. Naldoni, A. et al. Effect of nature and location of defects on bandgap narrowing in black TiO_2 nanoparticles. *J. Am. Chem. Soc.* **134**, 7600–7603 (2012).
12. Liu, N. et al. Black TiO_2 nanotubes: cocatalyst-free open-circuit hydrogen generation. *Nano Lett.* **14**, 3309–3313 (2014).
13. Zhou, W. et al. Ordered mesoporous black TiO_2 as highly efficient hydrogen evolution photocatalyst. *J. Am. Chem. Soc.* **136**, 9280–9283 (2014).
14. Liu, N. et al. Hydrogenated anatase: strong photocatalytic dihydrogen evolution without the use of a co-catalyst. *Angew. Chem. Int. Ed.* **53**, 14201–14205 (2014).
15. Zhang, L., Miller, B. K. & Crozier, P. A. Atomic level in situ observation of surface amorphization in anatase nanocrystals during light irradiation in water vapor. *Nano Lett.* **13**, 679–684 (2013).
16. Lu, Y. et al. Self-hydrogenated shell promoting photocatalytic H_2 evolution on anatase TiO_2. *Nat. Commun.* (in the press).
17. Van Duin, A. C. T., Dasgupta, S., Lorant, F. & Goddard, W. A. ReaxFF: a reactive force field for hydrocarbons. *J. Phys. Chem. A* **105**, 9396–9409 (2001).
18. Liang, T. et al. Reactive potentials for advanced atomistic simulations. *Annu. Rev. Mater. Res.* **43**, 109–129 (2013).
19. Senftle, T. P. et al. The ReaxFF reactive force-field: development, applications and future directions. *npj Comput. Mater.* **2**, 15011 (2016).
20. Car, R. & Parrinello, M. Unified approach for molecular dynamics and density-functional theory. *Phys. Rev. Lett.* **55**, 2471–2474 (1985).
21. Reuter, K. & Scheffler, M. Composition, structure, and stability of RuO_2(110) as a function of oxygen pressure. *Phys. Rev. B* **65**, 35406 (2001).
22. Zhao, X., Selcuk, S. & Selloni, A. Formation and stability of reduced TiO_x layers on anatase TiO_2(101): identification of a novel Ti_2O_3 phase. *Phys. Rev. Mater.* **2**, 15801 (2018).
23. Aschauer, U. & Selloni, A. Hydrogen interaction with the anatase TiO_2(101) surface. *Phys. Chem. Chem. Phys.* **14**, 16595–16602 (2012).
24. Gong, X.-Q., Selloni, A., Batzill, M. & Diebold, U. Steps on anatase TiO_2(101). *Nat. Mater.* **5**, 665–670 (2006).
25. Selcuk, S. & Selloni, A. Facet-dependent trapping and dynamics of excess electrons at anatase TiO_2 surfaces and aqueous interfaces. *Nat. Mater.* **15**, 1107–1112 (2016).
26. Yu, J., Low, J., Xiao, W., Zhou, P. & Jaroniec, M. Enhanced photocatalytic CO_2-reduction activity of anatase TiO_2 by coexposed {001} and {101} facets. *J. Am. Chem. Soc.* **136**, 8839–8842 (2014).
27. Tachikawa, T., Yamashita, S. & Majima, T. Evidence for crystal-face-dependent TiO_2 photocatalysis from single-molecule imaging and kinetic analysis. *J. Am. Chem. Soc.* **133**, 7197–7204 (2011).
28. De Angelis, F., Di Valentin, C., Fantacci, S., Vittadini, A. & Selloni, A. Theoretical studies on anatase and less common TiO_2 phases: bulk, surfaces, and nanomaterials. *Chem. Rev.* **114**, 9708–9753 (2014).
29. Scheiber, P. et al. (Sub)surface mobility of oxygen vacancies at the TiO_2 anatase (101) surface. *Phys. Rev. Lett.* **109**, 136103 (2012).
30. Cheng, H. & Selloni, A. Energetics and diffusion of intrinsic surface and subsurface defects on anatase TiO_2 (101). *J. Chem. Phys.* **131**, 1–10 (2009).
31. Claus, J., Leonhardt, M. & Maier, J. Tracer diffusion and chemical diffusion of oxygen in acceptor doped $SrTiO_3$. *J. Phys. Chem. Solids* **61**, 1199–1207 (2000).
32. Barnabel, V. I. & Bogomolov, V. N. Diffusion of defects in rutile during its partial reduction in a vacuum. *Sov. Phys. Solid State* **11**, 2160 (1970).
33. Barnard, A. S. & Curtiss, L. A. Prediction of TiO_2 nanoparticle phase and shape transitions controlled by surface chemistry. *Nano Lett.* **5**, 1261–1266 (2005).
34. Asahi, R., Taga, Y., Mannstadt, W. & Freeman, A. J. Electronic and optical properties of anatase TiO_2. *Phys. Rev. B* **61**, 7459–7465 (2000).
35. Yang, H. G. et al. Anatase TiO_2 single crystals with a large percentage of reactive facets. *Nature* **453**, 638–641 (2008).
36. Liu, G. et al. Titanium dioxide crystals with tailored facets. *Chem. Rev.* **114**, 9559–9612 (2014).
37. Wang, G. et al. Computational and photoelectrochemical study of hydrogenated bismuth vanadate. *J. Phys. Chem. C.* **117**, 10957–10964 (2013).

Acknowledgements

This work was supported by DoE-BES, the Division of Chemical Sciences, Geosciences and Biosciences under award DE-FG02-12ER16286. We used the resources of the National Energy Research Scientific Computing Center (DoE contract number DE-AC02-05CH11231). We also acknowledge use of the TIGRESS High Performance Computer Center at Princeton University.

Author contributions

A.S. initiated and supervised this research project. S.S. designed the models and the computational approaches, and performed the simulations, their analysis and visualization. X.Z. performed and analysed the DFT cluster calculations of the electronic properties. All authors contributed to discussions and writing the manuscript.

Competing interests

The authors declare no competing interests.

Additional information

Supplementary information is available for this paper at https://doi.org/10.1038/s41563-018-0135-0.

Reprints and permissions information is available at www.nature.com/reprints.

Correspondence and requests for materials should be addressed to S.S. or A.S.

Publisher's note: Springer Nature remains neutral with regard to jurisdictional claims in published maps and institutional affiliations.

Methods

First-principles calculations were performed using the PBE functional[38] with Hubbard U correction of 3.9 eV for Ti 3*d* orbitals[39], as implemented in the Quantum Espresso[40] package. We described electron–ion interactions using ultrasoft pseudo-potentials[41] with a 25.0 Ry (200.0 Ry) cut-off for the expansion of wavefunctions (augmented charge density). Only the Γ-point was used for Brillouin zone integrations. The surface was modelled using a 5-layer 1 × 3 anatase (101) slab; H atoms were adsorbed at the bridging surface O sites (O_{br}) to calculate the surface adsorption energies. To study V_O formation, surface O_{br} atoms were removed. Surface stability diagrams in H_2 and mixed H_2/H_2O atmosphere were determined using ab initio thermodynamics[21], with thermodynamics data for H_2, H_2O and O_2 taken from the NIST/JANAF webbook[42]. Details of cluster models used to calculate the DOS of the spherical nanoparticles are provided in the Supplementary Information.

We prepared the slab models for the classical molecular dynamics simulations by truncation of the anatase bulk structure. The a-101 slab model had dimensions $4.08 \times 4.17 \times 4.72\ nm^3$ and a total of 7,392 atoms (4 × 11 × 14 unit cells), the a-100 slab had dimensions $3.75 \times 4.18 \times 4.37\ nm^3$ and a total of 6,336 atoms, and the a-001 slab had dimensions $4.17 \times 4.17 \times 4.57\ nm^3$ and a total of 7,260 atoms. To build the spherical nanoparticle, we chose a Ti atom as the origin, and we truncated the bulk anatase structure to keep only the atoms within 3 nm of that centre. We then removed the singly coordinated O atoms and introduced two-coordinated O atoms wherever possible to reduce the number of undercoordinated Ti atoms. The resulting structure has 9,947 atoms with a variable radius of between 3 and 3.2 nm. It is slightly non-stoichiometric (chemical formula of $TiO_{1.9934}$) and exposes only four and five coordinated Ti atoms as undercoordinated surface atoms. The faceted diamond-like nanoparticle was truncated from the bulk so as to expose almost exclusively 101 facets; the resulting structure contains 5,311 atoms with the chemical formula $TiO_{1.9989}$. Another faceted nanoparticle, the truncated nanoparticle, was obtained by truncating the diamond-like nanoparticle so as to expose {001} facets (see Supplementary Fig. 14); the resulting structure contains 3,449 atoms with the chemical formula $TiO_{1.9861}$.

The ReaxFF molecular dynamics simulations were performed using LAMMPS[43,44] with a force field[45] that has been used to study the TiO_2–water interface[46,47]. Validation tests of this ReaxFF for the study of hydrogen and V_O diffusion in anatase are reported in Supplementary Figs. 1 and 2. Initial TiO_2 structures in H_2 atmosphere were prepared starting from separately equilibrated TiO_2 and H_2 models. We used a Nosé–Hoover style thermostat/barostat at desired temperature and pressure[48], and a time integration step of 0.1 fs.

Data availability. The data that support the results of this study are available from the corresponding authors upon reasonable request.

References

38. Perdew, J. P., Burke, K. & Ernzerhof, M. Generalized gradient approximation made simple. *Phys. Rev. Lett.* **77**, 3865–3868 (1996).
39. Anisimov, V. I., Zaanen, J. & Andersen, O. K. Band theory and Mott insulators: Hubbard U instead of Stoner I. *Phys. Rev. B* **44**, 943–954 (1991).
40. Giannozzi, P. et al. QUANTUM ESPRESSO: a modular and open-source software project for quantum simulations of materials. *J. Phys. Condens. Matter* **21**, 395502 (2009).
41. Vanderbilt, D. Soft self-consistent pseudopotentials in a generalized eigenvalue formalism. *Phys. Rev. B* **41**, 7892–7895 (1990).
42. Burgess, D. R. in *NIST Chemistry WebBook* (eds Linstrom, P. J. & Mallard, W.G.) (NIST, 2017); https://doi.org/10.18434/T4D303
43. Plimpton, S. Fast parallel algorithms for short-range molecular dynamics. *J. Comput. Phys.* **117**, 1–19 (1995).
44. Aktulga, H. M., Fogarty, J. C., Pandit, S. A. & Grama, A. Y. Parallel reactive molecular dynamics: numerical methods and algorithmic techniques. *Parallel Comput.* **38**, 245–259 (2012).
45. Kim, S. Y. et al. Development of a ReaxFF reactive force field for titanium dioxide/water systems. *Langmuir* **29**, 7838–7846 (2013).
46. Huang, L., Gubbins, K. E., Li, L. & Lu, X. Water on titanium dioxide surface: a revisiting by reactive molecular dynamics simulations. *Langmuir* **30**, 14832–14840 (2014).
47. Raju, M., Van Duin, A. C. T. & Fichthorn, K. A. Mechanisms of oriented attachment of TiO_2 nanocrystals in vacuum and humid environments: reactive molecular dynamics. *Nano Lett.* **14**, 1836–1842 (2014).
48. Tuckerman, M. E., Alejandre, J., López-Rendón, R., Jochim, A. L. & Martyna, G. J. A Liouville-operator derived measure-preserving integrator for molecular dynamics simulations in the isothermal-isobaric ensemble. *J. Phys. A.* **39**, 5629–5651 (2006).